VIII International Conference on Fracture Mechanics of Concrete and Concrete Structures
FraMCoS-8
J.G.M. Van Mier, G. Ruiz, C. Andrade, R.C. Yu and X.X. Zhang (Eds)

COMPUTATIONAL SIMULATION OF REINFORCED CONCRETE USING THE MICROPOLAR PERIDYNAMIC LATTICE MODEL

WALTER H. GERSTLE[*], HOSSEIN HONARVAR GHEITANBAF[*] AND AZIZ ASADOLLAHI[*]

[*] University of New Mexico
Department of Civil Engineering, University of New Mexico, Albuquerque, NM, USA
e-mail: gerstle@unm.edu, web page: http://www.unm.edu/~gerstle/

Key words: Peridynamic, Lattice, Reinforced Concrete, Simulation, Hexagonal, Micropolar

Abstract: The micropolar peridynamic lattice model for the simulation of plain and reinforced concrete structures is described and then demonstrated. It is found that the computational model is simpler than previous computational models for reinforced concrete, and more efficacious than existing computational methods for predicting the strength of reinforced concrete structures.

1 INTRODUCTION

The purpose of this paper is to demonstrate how the micropolar peridynamic lattice model (MPLM) can be used to predict the strength of reinforced concrete structures under quasistatic loading conditions. The MPLM has been introduced in [1].

In common behavioral regimes, continuum mechanics is an unsatisfactory model for reinforced concrete structures, because the concrete deformation, even prior to failure, is discontinuous. Silling's peridynamic model [2] has not entirely discarded the continuum paradigm, because the material space continues to be idealized as continuous, and thus the original peridynamic model requires that further discretization decisions be made for the model to be computationally evaluated.

We discard the continuum material concept completely, and regard the concrete as a discrete lattice of particles. By using close-packed particle lattices in 1D, 2D and 3D, the MPLM has the potential to simulate the major features of quasibrittle materials, including elasticity, anisotropic damage, fracture, and even plasticity. Typically, lattice models have viewed the structure as a collection of beam or truss elements connected together at nodes (as with traditional truss- and beam-analogy lattice models). On the other hand, the MPLM views the structure as a collection of interacting point masses (as with the peridynamic and discrete element models). The material constitutive behavior is captured via inter-particle forces and moments that are functions of particle positions and velocities and their histories [3]. In the reference configuration, the MPLM uses a finite number of regularly-spaced interacting particles of finite mass, rather than an infinite number of infinitesimal particles as with peridynamics. Additionally, the MPLM is conceptually simpler than the original peridynamic model, and more general than the traditional beam-lattice models, not to mention classical finite element methods.

After defining the MPLM, a constitutive model for concrete is developed and calibrated, and its use is demonstrated using several two-dimensional example problems. Then, a model for reinforcing steel and a model for bond between the steel and the concrete is introduced. Finally, reinforced concrete beams are simulated and conclusions are drawn.

2 MICROPOLAR PERIDYNAMIC LATTICE MODEL (MPLM)

Fig. 1 shows a 2D close-packed particle lattice. Each particle is spaced a distance, *s*, from its six nearest neighbors.

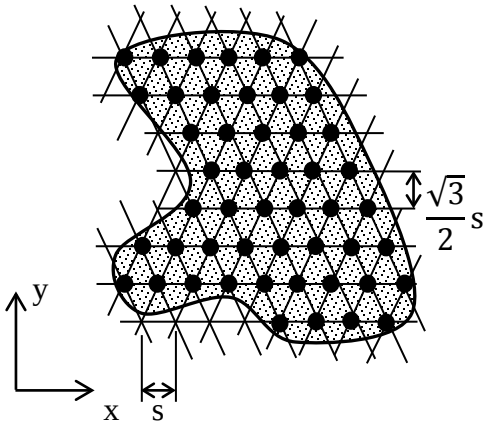

Figure 1: Two-dimensional hexagonal lattice.

The volume per particle is $\Delta V = \frac{\sqrt{3}}{2} s^2 t$ for a 2D hexagonal lattice representing a flat plate of thickness, t. To represent a material with a mass density of ρ, each particle is endowed with a mass of $\Delta m = \rho \Delta V$. Assuming that each particle is a uniform solid sphere with radius, $r \approx \frac{s}{2}$, its mass moment of inertia, ΔI, identical about all axes through the particle, is $\Delta I = \frac{2}{5} m r^2$.

The particle lattice spacing, *s*, can reasonably be chosen as the material grain characteristic size (such as the maximum aggregate size for concrete). Alternately particle spacing, *s*, may be chosen based upon the requirement that the number of particles used for a particular problem not exceed the capacity of the computational resource. For a material like concrete, it makes no sense to allow the particle lattice spacing to be less than the aggregate size; the mesoscale of the material sets a lower bound on appropriate lattice particle spacing, *s*. Indeed, it makes no sense to define geometric features that are smaller than the aggregate size, as even if a structure with such small features could be constructed, these tiny features could hardly be considered as consisting of a spatially homogenous material. Thus, in contrast with traditional continuous R^3 geometry, within the MPLM, a "perfectly sharp crack" and a "perfectly sharp corner" are meaningless features, impossible to express. Thus the MPLM is a suitable geometric model for materials with a grain size that is not too much smaller than the characteristic dimensions of the structure – and where powerful computers are available.

With the material mass represented by particles in a lattice, Newton's second law of motion is applied to each particle, *i*:

$$\sum_{j=1}^{N_i} \boldsymbol{F_{ij}} + \boldsymbol{F_{exti}} = \Delta m \ddot{\boldsymbol{u}}_i, \text{ and} \quad (1)$$

$$\sum_{j=1}^{N_i} \boldsymbol{M_{ij}} + \boldsymbol{M_{exti}} = \Delta I \ddot{\boldsymbol{\theta}}_i, \quad (2)$$

where $\boldsymbol{F_{ij}}$ and $\boldsymbol{M_{ij}}$ are the force and moment vectors, respectively, exerted by particle *j* on particle *i*, $\boldsymbol{F_{exti}}$ and $\boldsymbol{M_{exti}}$ are the externally applied force and moment vectors, respectively, applied to the centroid of particle *i*, and $\ddot{\boldsymbol{u}}_i$ and $\ddot{\boldsymbol{\theta}}_i$ are the linear and angular acceleration vectors, respectively, of the centroid of particle *i*. N_i is the number of particles, *j*, that are within the spherical neighborhood, whose radius is the "material horizon", δ, of particle *i*. With a close-packed lattice, and $\delta = 1.5s$, N_i is six (or less) for a 2D problem. Of course, one could contemplate MPLM models with larger material horizons, which might be preferable from the point of view of producing isotropic damage behavior with respect to lattice orientation, but the number of neighboring particles, N_i, and thus the number of force computations would be larger, per particle.

Equations 1 and 2 are integrated explicitly in time using the velocity Verlet integration method, with time step, $\Delta t = s/(n \times c_0)$, with *s* being the particle spacing, c_0 being the speed of sound in the material, and n being π or greater for stability. Because we are interested in modeling cementitious materials, with highly nonlinear material behavior, explicit time integration is the method of choice.

The vector functions $\boldsymbol{F_{ij}}$ and $\boldsymbol{M_{ij}}$ describe the internal forces and moments between neighboring lattice particles, and from these

functions, the material behavior emerges. For a bond-based micropolar peridynamic model, $\boldsymbol{F_{ij}}$ and $\boldsymbol{M_{ij}}$ are chosen to be functions of the reference position vectors, $\boldsymbol{x_{0i}}$ and $\boldsymbol{x_{0j}}$, and current position vectors, $\boldsymbol{x_{ti}}$ and $\boldsymbol{x_{tj}}$, and also as functions of the velocities $\boldsymbol{v_{ti}}$ and $\boldsymbol{v_{tj}}$ of particles *i* and *j*. Note that all of these kinematic vectors include particle positions (and velocities) as well as particle rotations (and angular velocities). The functions $\boldsymbol{F_{ij}}$ and $\boldsymbol{M_{ij}}$ also depend upon evolving damage parameters, ω_{ij}, associated with the interaction between particle *i* and particle *j*.

For a state-based peridynamic model [4], vectors $\boldsymbol{F_{ij}}$ and $\boldsymbol{M_{ij}}$ may be functions not only of the states of particles *i* and *j*, but also of all other particle, *k*, states and interaction damage states, ω_{ik}, within the peridynamic horizon of particle *i*.

With today's high performance parallel computers, a million particles can reasonably be modeled, and for concrete with aggregate size of 2 cm, a volume of $(0.02m)^3/particle \times 1{,}000{,}000\ particles = 8m^3$ of concrete for at least several fundamental vibration periods can be simulated. Thus, on a parallel computer, it is feasible to simulate large 3D concrete structures using the MPLM – not just small laboratory specimens.

In solid models, the forces between particles are assumed to arise due to deviations from a reference state. As long as the deviation of particle positions from their reference locations is not too extreme, the MPLM is suitable. Taking the terminology "cohesive crack model" to its logical conclusion, the MPLM could perhaps be termed a "cohesive particle" model.

3 MPLM MODEL FOR CONCRETE

A MPLM constitutive model for concrete is proposed in this section. Others are certainly possible. We start with the linear elastic regime.

3.1 MPLM linear elasticity

If the interaction between two particles spaced at distance *s* is thought of as a linear elastic Euler-Bernoulli frame element with axial stiffness a=E'A and bending stiffness b=E'I, then to simulate a plane-stress elastic continuum of thickness t and with Young's modulus E and Poisson's ratio, ν, the formulas for a and b are given by

$$a = \frac{Est}{\sqrt{3}(1-\nu)} \text{ and } b = \frac{Es^3(1-3\nu)t}{12\sqrt{3}(1-\nu^2)}\ . \tag{3}$$

Similar expressions for 1D, 2D plane strain, and 3D continua are found in [5]. In our computational formulation, elastic interaction deformations (interaction stretches and curvatures) are assumed to be reasonably small, but large translations and rotations are accounted for using a co-rotational stiffness formulation [6; 7]. Thus, patches of particles can detach as rigid bodies and move correctly with large translations and rotations. However, particle collision behavior is not currently incorporated into the model, except between particles that are adjacent in the reference lattice.

While the presented linear elasticity model gives the same results as the classical Navier-Cauchy elasticity model for states of uniform strain far from boundaries, it yields slightly different results than the classical elasticity model in the presence of nonuniform strain fields and near boundaries. This does not make the MPLM model wrong; just slightly different than the Navier-Cauchy continuum model. One could argue that the MPLM elasticity model is more realistic than the classical Navier-Cauchy model for materials like concrete.

3.2 MPLM damage model

With reference to Fig. 2, the micropolar axial stretch of interaction *ij*,

$$\epsilon_a \equiv \frac{d_t - d}{d}, \tag{4}$$

where d_t is the current length and d is the reference length, is defined in a manner similar to axial strain.

Similarly, the maximum micropolar

curvatures about the local *z*-, *y*- and *x*-axes, respectively, of interaction *i j* are:

$$\psi_z \equiv max\begin{bmatrix}\left|\frac{2}{d}\left(2\theta_z^i+\theta_z^j-\frac{3}{d}\left(d_y^j-d_y^i\right)\right)\right|,\\ \left|\frac{2}{d}\left(2\theta_z^j+\theta_z^i-\frac{3}{d}\left(d_y^i-d_y^j\right)\right)\right|\end{bmatrix}, \quad (5)$$

$$\psi_y \equiv max\begin{bmatrix}\left|\frac{2}{d}\left(2\theta_y^i+\theta_y^j-\frac{3}{d}\left(d_z^j-d_z^i\right)\right)\right|,\\ \left|\frac{2}{d}\left(2\theta_y^j+\theta_y^i-\frac{3}{d}\left(d_z^i-d_z^j\right)\right)\right|\end{bmatrix}, \text{ and } \quad (6)$$

$$\psi_x \equiv \left|\frac{\theta_x^j-\theta_x^i}{d}\right| . \quad (7)$$

We propose measures of micropolar tensile and compressive interaction deformation as

$$\epsilon_{mp+} \equiv \epsilon_a + \beta d\sqrt{{\psi_x}^2+{\psi_y}^2+{\psi_z}^2} \text{ and} \quad (8)$$

$$\epsilon_{mp-} \equiv \epsilon_a - \beta d\sqrt{{\psi_x}^2+{\psi_y}^2+{\psi_z}^2} , \quad (9)$$

where β is a dimensionless parameter.

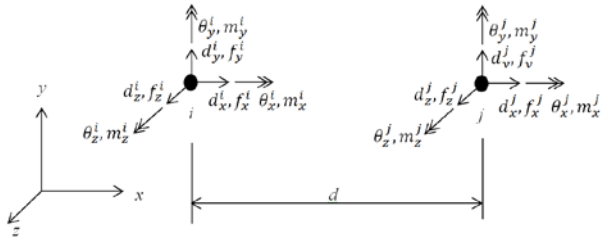

Figure 2: Displacement and force components, in local coordinates, acting between particles *i* and *j*, separated by reference distance, *d*.

The tensile damage parameter, ω_t, is defined in terms of these deformation measures, with reference to Fig. 3, as:

for tension damage:

$$\text{for } 0 \le \epsilon_{mp+} \le \epsilon_t, \quad \omega_t = max(0, \omega_{tprev}) \quad (10)$$

$$\text{for } \epsilon_t \le \epsilon_{mp+} \le \alpha_t\epsilon_t, \quad \omega_t = max(\Omega_t(\epsilon_{mp+}), \omega_{tprev}) \text{ and} \quad (11)$$

$$\text{for } \alpha_t\epsilon_t \le \epsilon_{mp+}, \quad \omega_t = 1 , \quad (12)$$

where ω_{tprev} is the value of the tensile damage parameter for interaction *ij* in the immediately preceding time step. The damage function $\Omega_t(\epsilon_{mp+})$ is defined in Fig. 3(a), and it has been chosen in such a way that the cohesive tensile softening behavior is modeled approximately correctly.

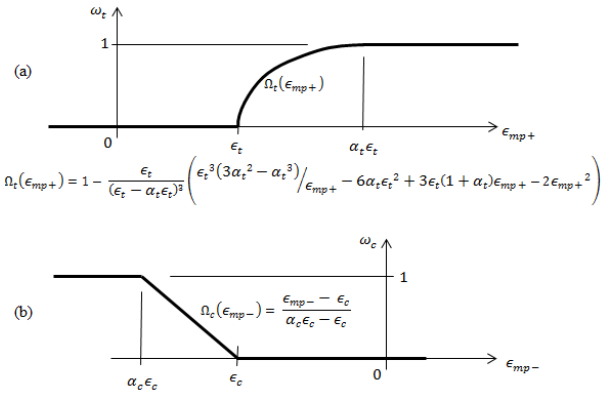

Figure 3: (a) Damage, ω_t, versus the micropolar strain measure, ϵ_{mp+}. (b) Damage, ω_c, versus the micropolar strain measure, ϵ_{mp-}. (ω_t and ω_c never decrease with time.)

For the evolution of compression damage, ω_c:

$$\text{for } \epsilon_{mp-} \le \alpha_c\epsilon_c , \quad \omega_c = 1 \quad (13)$$

$$\text{for } \alpha_c\epsilon_c \le \epsilon_{mp-} \le \epsilon_c , \quad \omega_c = \max(\Omega_c(\epsilon_{mp-}), \omega_{cprev}) \text{ and} \quad (14)$$

$$\text{for } \epsilon_c \le \epsilon_{mp-}, \quad \omega_c = \max(0, \omega_{cprev}), \quad (15)$$

where ω_{cprev} is the value of the compressive damage parameter for interaction *ij* in the immediately preceding time step. Function $\Omega_c(\epsilon_{mp-})$ is defined in Fig. 3(b).

The damage parameter, ω, is computed as the maximum of ω_t and ω_c.

If $\epsilon_a \ge 0$, then

$$\{f\}=(1-\omega)[K]\{d\} , \quad (16)$$

and if $\epsilon_a \le 0$, then

$$\{f\}=(1-\omega)[K^*]\{d\} , \quad (17)$$

where $\{f\}$ is the force vector acting between

particles *i* and *j*, *[K]* is the elastic stiffness matrix defined using Eq. 3, and *{d}* is the vector of particle deformations, associated with interaction *ij*. Because there are many interactions per particle, this form allows damage to be anisotropic.

With the stiffness matrix, $[K^*]$, the axial components of force are the same as that computed by *[K]*, but the shears and moments are reduced by the damage parameter $(1-\omega)$. Thus, compression failure is indirectly precipitated by loss of moment and shear capacity (and subsequent instability due to nonlinear geometric effects), but not by loss of axial stiffness.

In this implementation, damage can be either tensile or compressive, but not both.

The constitutive model presented has eight parameters: peridynamic lattice spacing parameter *s*, micro-elastic stiffness parameters *a* and *b*, and the parameters governing tensile and compressive damage evolution: ϵ_t, α_t, ϵ_c, α_c, and β.

The lattice spacing parameter, *s*, is chosen to be as small as the available computational capacity allows, but no less than the largest material grain size.

The parameter ϵ_t is calibrated to reproduce the tensile strength, f_t, of the concrete: $\epsilon_t \approx \frac{f_t}{E}$.

The parameter, $\beta \approx 0.1$, is chosen to replicate the ratio of uniaxial compressive load to uniaxial tensile load, usually around ten, as is observed empirically for normal-strength concrete.

The parameter $s_c \approx 0.001$ is chosen to replicate the strain at which uniaxial compressive failure commences, and $\alpha_c s_c \approx 0.003$ is chosen to represent the ultimate compressive strain.

The parameter α_t is chosen to replicate the tensile fracture energy, G_F, of the material, as described in [1].

3.3 MPLM frictional model

The frictional model requires that when the link is in axial compression ($\epsilon_a \leq 0$), and when $\omega = 1$ the magnitude of the shear force ($f_y^i = -f_y^j$) must never exceed the internal coefficient of friction, μ, times the compressive axial force ($f_x^i = -f_x^j$). For equilibrium with the shear force, the moments are computed as $m_z^i = m_z^j = \frac{df_y^i}{2}$.

3.4 MPLM damping model

Damage events can release sudden bursts of acoustic energy. If no material damping is included in the model, this acoustic energy can cause spurious vibration and consequent damage. Thus we incorporate an axial peridynamic damping model. When computing the force in interaction *ij*, the relative axial velocity, v_{ij}, between particles *i* and *j* is computed. Then the axial damping force, f_{dampij}, between the two particles is given by

$$f_{dampij} = 2\zeta m\omega_n v_{ij}, \text{ and} \quad (18)$$

$$F_{ij} = f_{elastij} + f_{dampij}, \quad (19)$$

where ζ is the ratio of critical damping, with value set between 0 and 1, m is the particle mass, ω_n is the highest natural frequency of vibration, v_{ij} is the relative axial velocity between particles *i* and *j*, $f_{elastij}$ is the elastic inter-particle axial force calculated in the previous section, including the effect of damage, and F_{ij} is the internal axial force used in Eq. 1. The damping force, always opposing the direction of motion, removes energy from the system. We find that choosing $\zeta \approx 0.05$ produces reasonable damping behavior.

A similar strategy, not yet implemented and apparently not necessary, may be used to damp shear and rotational degrees of freedom.

4 MODELING OF REINFORCING BARS AND BOND

A reinforcing bar is represented as a 1D lattice of MPLM particles representing a bar with cross-sectional area A_s and cross-sectional moment of inertia I_s. The material parameters are Young's modulus E_s and yield stress F_y. Steel particles interact if they spaced less than *s* from each other. Steel particles from separate reinforcing bars do not interact.

As shown in Fig. 4, only every other steel

particle of a given rebar is connected to concrete particles within a horizon *s* using the same elastic interaction model as for concrete-concrete particles (such interactions assume no damage). The reason that only every other steel particle is connected to concrete is to allow cracks in concrete to develop unhindered by the non-damaged steel-concrete interactions. If the distance between a steel particle and a concrete particle is zero, the interaction between these two particles is ignored.

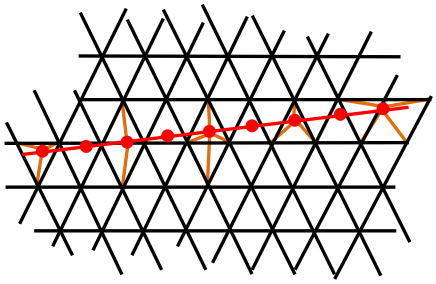

Figure 4: Bond of reinforcement (red) to concrete (black) using peridynamic interactions (tan).

Bond-slip is indirectly modeled and emerges from the elasticity and damage of the interactions between surrounding the concrete particles.

5 EXAMPLES

In all of the following examples, the target classical materials parameters are shown in Table 1, and the corresponding selected MPLM parameters for concrete and steel are shown in Tables 2 and 3. The time step is chosen as $\Delta t = \frac{s}{24c_{0(steel)}} = 1.808 \times 10^{-7}\ s$. In each example, the load is linearly ramped from zero to the peak load for duration of at least four fundamental periods of the structure, and is thus essentially quasistatic. The load is ramped from time zero up to 75% of the total simulation time and then held constant.

"Strength" is defined as the peak load at which static equilibrium can still be achieved.

In all of the following examples, the particles in the deformed configuration are shown and the damaged interactions are color-coded as shown in Fig. 5. Undamaged interactions are not shown in the figures.

The steel-concrete MPLM interactions are identical to concrete-concrete interactions, except that they are assumed to be linear elastic, with no damage. The steel is modeled as elastic-perfectly plastic.

Table 1: Classical material parameters

Parameter	Value	Units
Conc. Young's modulus, E_c	24.86	GPa
Conc. Poisson's ratio, μ_c	0.20	-
Conc. comp. strength, f'_c	27.58	MPa
Conc. tens. strength, f_t	2.758	MPa
Conc. Density, ρ_c	2323.0	kg/m^3
Conc. fracture toughness, G_F	175.0	N/m
Steel Young's modulus, E_s	200.0	GPa
Steel yield strength, F_y	414.0	MPa
Steel Poisson's ratio, μ_s	0.3	MPa
Steel Density, ρ_s	7850.0	kg/m^3

Table 2: MPLM parameters for concrete

Parameter	Value	Units
Lattice Spacing, s	0.020	m
Microelastic parameter, a	4.557×10^7	N
Microelastic parameter, b	506.3	$N\text{-}m^2$
Tensile stretch limit S_t	0.000126	-
Tensile stretch ratio α_t	10	-
S_c	-0.001	-
α_c	5.728	-
β	0.10	-
Damping ratio, c	0.05	-

Table 3: MPLM parameters for steel

Parameter	Value	Units
Lattice Spacing, s	0.020	m
Microelastic parameter, a	E_sA_s	N
Microelastic parameter, b	E_sI_s	$N\text{-}m^2$
Yield limit, S_t	0.00207	-
Damping ratio, c	0.05	-

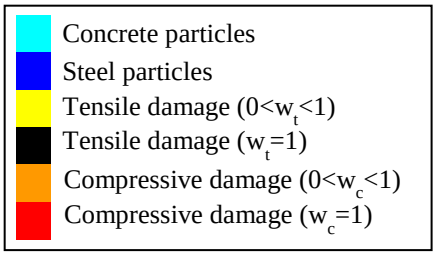

Figure 5: Color-coding for example problems.

5.1 Uniaxial tension

Fig. 6 shows the deformed particles for two uniaxial tension examples, with the load direction in Fig. 6(b) rotated by 90^o with respect to the lattice in Fig. 6(a). Equal tensile loads are applied to each of the particles in the end two layers of particles; similarly, opposite forces are applied to the two layers of particles on the opposite end of the specimen. The total number of simulation time steps is 10000. The damage patterns in each specimen at the end of the simulation are shown in Fig. 6. For the lattice orientation in Fig. 6(a), the failure load is at a stress level of 2.784 MPa (within 1% of the target f_t). However, for the lattice orientation in Fig. 6(b), the failure load is at a stress level of 3.226 MPa (17% higher than the target f_t). Thus, although the character of the damage patterns is reasonable in both cases, we conclude that the tensile strength is somewhat sensitive to lattice orientation. Significant tensile damage (yellow) is evident prior to crack formation (black).

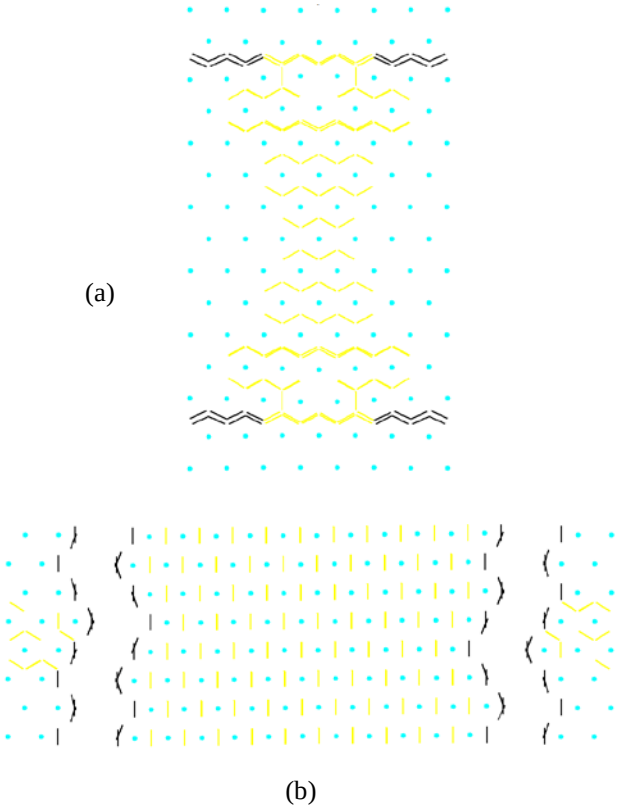

Figure 6: Damage patterns for uniaxial tension. Deformations magnified by factor of 100, at time step 10000. (a) Load applied in vertical direction; (b) Load applied in horizontal direction.

5.2 Uniaxial compression

To investigate uniaxial compressive behavior, the problem described in Section 5.1 is repeated, but now the loading directions are reversed. The resulting deformed configurations and damage patterns are shown in Figs. 7(a) and (b) for two loading directions with respect to the lattice orientation.

For the lattice orientation in Fig. 7(a), the failure load is at a stress level of 28.48 MPa (3.3% higher than the target f'_c). However, for the lattice orientation in Fig. 7(b), the failure load is at a stress level of 61.06 MPa (121% higher than the target f'_c). As shown in Figs. 7(a) and 7(b), the tensile damage patterns between the two loading orientations are similar, but the compressive damage patterns are different. We conclude that both the compressive strength and failure mode are sensitive to lattice orientation. Further study and innovation are indicated.

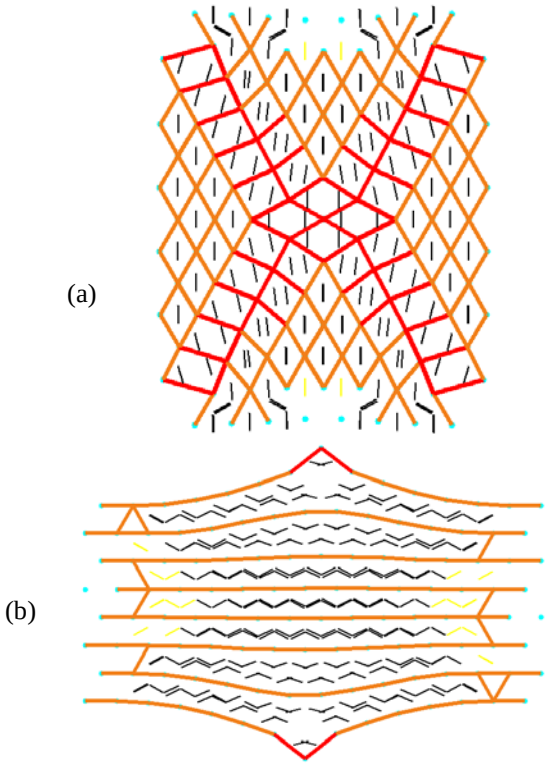

Figure 7: Damage patterns for uniaxial compression. Deformations magnified by factor of 10, at time step 10000. (a) Load applied in vertical direction; (b) Load applied in horizontal direction.

5.3 Plain beam

We assume a plane-stress uniformly-loaded beam, with span of 1.16 m, depth of 0.26 m, and thickness of 0.12 m. With reference to Fig. 8, each particle in the top layer of particles is loaded downward to simulate uniform loading. To apply the load approximately statically, the load is ramped linearly from time zero up to 75% of total simulation time and then the load is held steady. The simulation is run for 80000 time steps. Assuming, classically, that the beam's strength is achieved when the bending stress reaches tensile strength, f_t, the failure load is predicted as 22.14 kN/m. The MPLM simulation predicts a failure load 2.1 times higher than the classical failure load: 46.4 kN/m. This result is not unexpected: the modulus of rupture is typically around twice the tensile strength, especially for small beams. The deformed shape and the damage in the beam at failure are shown in Fig. 8. Note that the crack branches: perhaps a consequence of dynamic fracture.

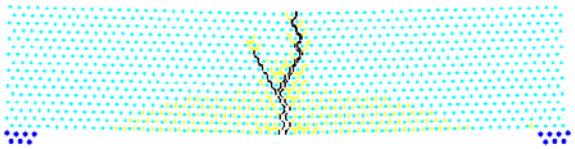

Figure 8: Deformed shape and damage in plain concrete beam subject to uniform loading at time step 80000. Deformation is magnified by factor of 10.

5.4 Reinforced beam with no stirrups

The plain beam in the previous section is now reinforced with a single horizontal steel reinforcing bar, of diameter 1.27 cm, whose centroid is located 2 cm above the bottom of the beam, as shown in Fig. 9. The beam is loaded as in the previous section. The simulation is run for 80000 time steps. According to the ACI code [8], the nominal bending strength of the singly-reinforced beam is 72.24 kN/m. The MPLM simulation predicts a slightly higher strength of 78.74 N/m. The deformed shape and associated damage are shown in Fig. 9.

The damage patterns look reasonably realistic, including secondary cracking at the bottom of the beam and some compression damage at the top of the beam. At time step 65000, the distributed damage above the reinforcing bar extending to the ends of the beam and the compression damage above the supports is somewhat unexpected and is perhaps an indication of bond failure.

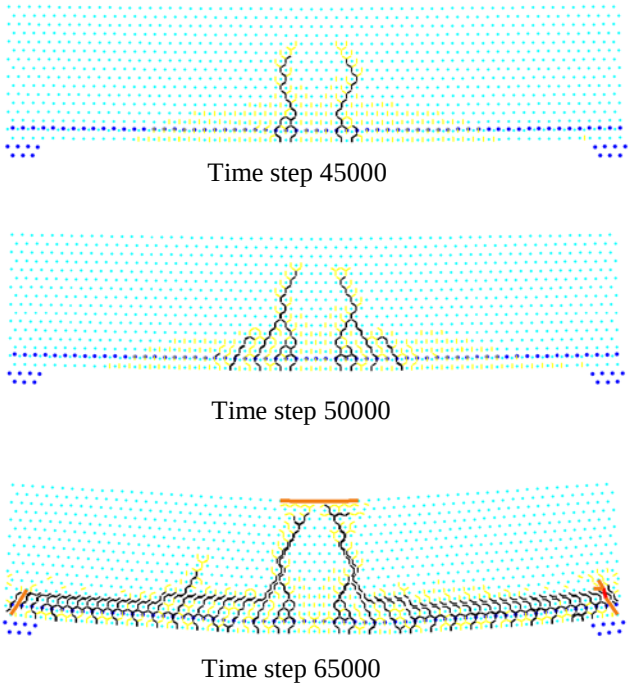

Figure 9: Deformed shape and damage in reinforced concrete beam subject to uniform loading. Deformation is magnified by factor of 10.

5.5 Reinforced beam with stirrups – bending failure

The plain beam in Section 5.3 is now reinforced with both flexural and the shear steel bars having diameters of 1.27 cm and 1.0 cm, respectively. The centroid of flexural steel is located 2.0 cm above the bottom of the beam. The centroid of left-most stirrup is positioned at 4 cm from the left end of the beam and the stirrup spacing is 8 cm. The ACI code [8] predicts a bending-type failure of 72.24 kN/m. The MPLM simulation is run for 80000 time steps. The MPLM simulation predicts strength of 68.63 kN/m. The deformed shape and damage in the beam are shown in Fig. 10 at three different stages of loading.

Surprisingly, by adding stirrups, the cracking behavior was altered significantly from the unreinforced beam, and the failure

load was slightly reduced. Perhaps the stirrups increased the bond strength, thus preventing bond failure in the beam without stirrups. More study is indicated.

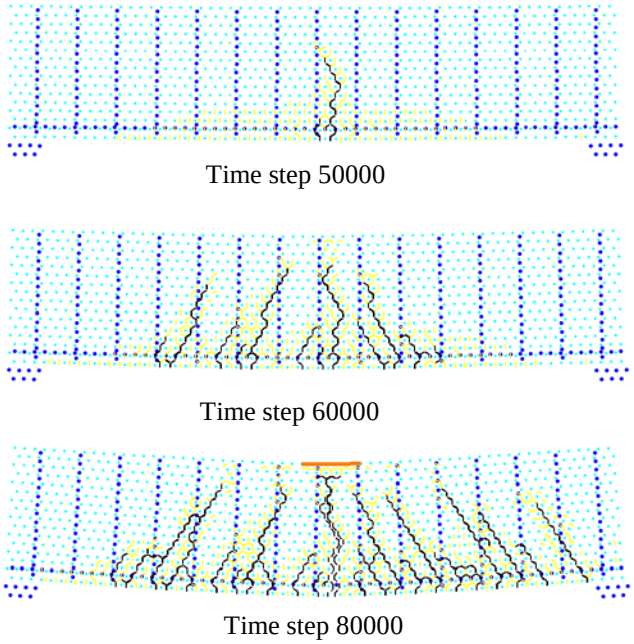

Figure 10: Deformed shape and damage in reinforced beam with stirrups. Deformations are magnified by factor of 10. Bending failure is indicated.

5.6 Reinforced beam with stirrups – shear failure

To increase the bending strength and thus induce a shear failure, the diameter of horizontal rebar in the previous section is now increased to 3.175 cm while keeping the stirrups unchanged. According to the ACI code [8], the failure is now of shear type, with a shear strength of 210 kN/m. The deformed shape and damage in the beam are shown in Fig. 11. The MPLM predicts a failure load of 252 kN/m, as expected, somewhat higher than the ACI prediction.

6 CONCLUSIONS

We have presented the micropolar peridynamic lattice model (MPLM) and have demonstrated its use in simulating several plain and reinforced concrete structures. While the MPLM, as here implemented, has been shown to be somewhat non-objective with respect to lattice rotation, it nonetheless predicts damage, fracture, and strength more directly and realistically than many existing computational methods. Additionally, the MPLM makes strength predictions that are similar to those of the ACI code [8].

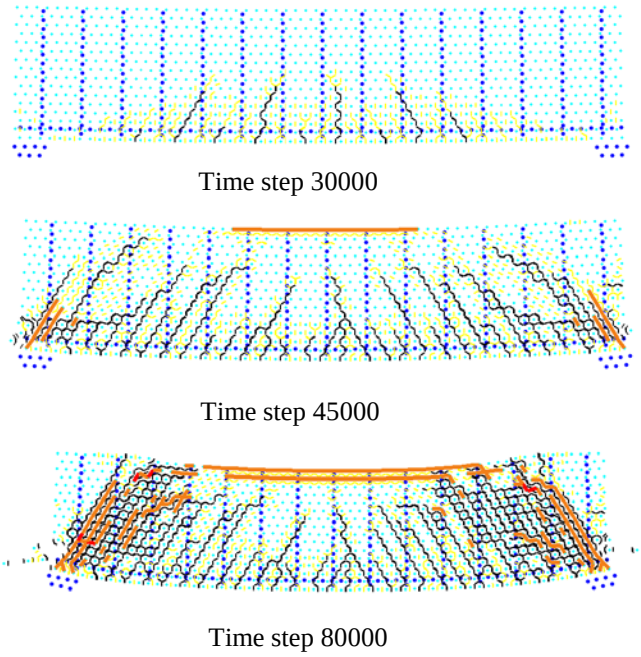

Figure 11: Deformed shape and damage in reinforced beam with stirrups. Deformations are magnified by factor of 10. Shear failure is indicated.

Non-objectivity with respect to lattice rotation could be reduced by increasing the peridynamic horizon to include more neighboring particles – but at increased computational cost.

All of the examples shown in this paper ran in under ten minutes on a single-processor computer. The model can be extended to 3D, but high-performance computers will be necessary to solve realistic 3D problems [9; 10].

Future improvements to the MPLM peridynamic constitutive model may improve its accuracy, efficiency, and usefulness.

One great advantage of the method is that it is conceptually simple, and therefore has the potential to allow practicing engineers to have sufficient confidence in the model to use it and thus to produce more rational designs.

REFERENCES

[1] Gerstle, W., Honarvar Gheitanbaf, H., Asadollahi, A., Tuniki, B.-K., and Rahman, A., 2012. “Simulation of concrete using micropolar peridynamic lattice model”, Computers and Structures, under review.

[2] Silling, S. 2000. “Reformulation of Elasticity Theory for Discontinuities and Long-Range Forces”. Journal of the Mechanics and Physics of Solids 48: 175-209.

[3] Gerstle, W.,Sau, N., and Aguilera, E., 2007. "Micropolar Peridynamic Constitutive Model for Concrete", 19th Intl. Conf. on Structural Mechanics in Reactor Technology (SMiRT 19), Toronto, Canada, August 12-17, pp. B02/1-2.

[4] Silling, S.A., Epton, M., Weckner, O., Xu, J., Askari, E. 2007. “Peridynamic States and Constitutive Modeling”, Journal of Elasticity, Vol. 88, Issue 2, pp. 151-184.

[5] Rahman, ASM. A. 2012. “Lattice-Based Peridynamic Modeling of Linear Elastic Solids” Master’s Thesis, University of New Mexico.

[6] Yaw. L. L., 2008. “Co-rotational Meshfree Formulation For Large Deformation Inelastic Analysis Of Two-Dimensional Structural Systems”. PhD thesis, Dept. of Civil and Environmental Engineering, UC Davis.

[7] Crisfield, M. A., 1991. “Nonlinear Finite Element Analysis of Solids and Structures”, Vol. 1, Wiley.

[8] ACI318, 2011. “Building Code Requirements for Structural Concrete”. American Concrete Institute.

[9] Gerstle, W. Sakhavand, N. and Chapman, S. 2010. “Peridynamic and continuum models of reinforced concrete lap splice compared”, Proceedings of the 7th International Conference on Fracture Mechanics of Concrete and Concrete Structures (FraMCoS-7), pp. 306-312.

[10] Sakhavand, N. 2011. “Parallel Simulation of Reinforced Concrete Structures using Peridynamics”, Master’s Thesis, University of New Mexico.